Advanced Intelligent Systems

ADVANCED INTELLIGENT SYSTEMS Open Access

www.advintellsyst.com

RESEARCH ARTICLE OPEN ACCESS

Motion and Morphology Planning for Autonomous Manipulation in Clutter With a Shape-Shifting, Variable-Stiffness Robot

Luiza Labazanova[1] | Liuming Qiu[1] | Jose Guadalupe Romero[2] | Li Cheng[1] | Thrishantha Nanayakkara[3] | David Navarro-Alarcon[1]

[1]The Hong Kong Polytechnic University, Kowloon, Hong Kong | [2]ITAM, Mexico City, Mexico | [3]Imperial College London, London, UK

Correspondence: David Navarro-Alarcon (dnavar@polyu.edu.hk)

Received: 1 December 2025 | **Revised:** 29 May 2026 | **Accepted:** 29 June 2026

Keywords: adaptive morphology | full-body grasping | mobile manipulation | motion planning | robot design | variable stiffness

ABSTRACT

Autonomous operation in confined spaces demands robots that can simultaneously navigate tight passages and manipulate objects. However, conventional mobile manipulators are often too large, while compliant soft manipulators are typically limited by tethers and a small operational workspace. This article introduces a novel hybrid robot designed to address this trade-off. The robot achieves mobile manipulation without dedicated end effectors by leveraging its entire body. It comprises two autonomous locomotion units linked by a Variable-Stiffness Bridge (VSB). This design enables transitions between a rigid state for efficient locomotion and a flexible state for full-body enclosure of objects. After enclosure, the robot re-stiffens to enable push-coupled planar transport with orientation regulation. We present the second iteration of this platform, featuring a modular VSB design that achieves a 2.5-fold increase in state transition speed. Furthermore, we introduce a comprehensive planning framework, the Voronoi-based Motion and Morphology Planner (VMMP), to enable autonomous navigation in highly cluttered planar environments. VMMP addresses the high-dimensional planning challenge through a hierarchical decomposition: it first uses Voronoi diagrams to generate traversable paths for three key control points on the robot's body and then reconstructs the kinematically feasible robot configuration sequence via constrained optimization. The source code and simulations are available at https://github.com/Louashka/2sr-robot.

1 | Introduction

Navigating and operating within unstructured environments present a formidable challenge for robotic systems. Many real-world scenarios, such as industrial inspection or search and rescue, demand systems that can retrieve objects in cluttered environments with limited access. To be effective, robots must combine robust locomotion with dexterous manipulation capabilities. Early attempts to integrate these functions led to solutions like mobile manipulators, which mount robotic arms on mobile bases [1, 2], or warehouse robots designed to lift and transport cargo [3]. However, these platforms are typically bulky and rely on rigid components, requiring carefully supervised workspaces specifically prepared for their operation.

Robots designed specifically for confined spaces typically follow two paths: compact sensor platforms [4, 5] or multi-legged systems for rough terrain [6, 7]. In either case, integrating manipulation capabilities is a significant challenge, as adding grippers or tools often compromises the robot's primary navigation and mobility functions. This challenge stems from conventional robotics' reliance on rigid components and fixed structures, which constrains functional versatility.

To overcome the constraints of rigid robotics, a paradigm shift toward adaptive morphology has gained significant traction, enabling the creation of multimodal and multifunctional systems [8–10]. This paradigm has manifested in several distinct research directions. One strategy involves reconfigurable truss architectures, where active control of elastic or jointed elements allows the robot to alter its own shape and passive mechanical properties [11, 12]. Such systems have demonstrated the ability to switch between locomotion modes like driving, rolling, and even swimming [13]. While promising, their range of shape change is often constrained, and their form factor can be too large to navigate narrow passages or perform fine-grained object interaction.

Another strategy involves modular robotics, which leverages collective behaviors from individual components. These systems achieve complex tasks through coupled mechanisms [14, 15], multi-agent coordination [16–18], or deformable chains [19–21]. The aggregate mechanics of these modules allow them to squeeze through tight spaces or envelop objects for transport. However, their locomotion is often slow or dependent on specialized environmental conditions, such as vibrating surfaces, which limits their real-world applicability.

The biggest departure from conventional design is found in soft robotics, whose inherent compliance and continuous deformation offer unparalleled adaptability to the environment [22, 23]. Soft robots excel at exploring constrained spaces like pipelines [24, 25], but often at the cost of payload capacity and force output. To address this, nature-inspired designs have emerged, such as inchworm-like [26] and ant-like [27] soft robots capable of both locomotion and grasping. Soft components can also augment other architectures; for instance, the truss robot Tetraflex [28] uses inflatable bellows to roll, crawl, and transport objects. A common limitation of soft robots is the need for an external pressure supply, which introduces a tether and restricts operating range. In response, substantial progress has been made toward untethered soft robotics, including systems that carry onboard pneumatic sources [29] and robots driven by alternative actuators such as shape-memory alloys [30]. However, removing the tether typically shifts the bottleneck to onboard energy/pressure storage, runtime, and sensing/control integration, which can force trade-offs in size, payload, and task duration. For example, isoperimetric robots developed by Usevitch et al. [31] operate at a relatively large scale (0.85 to 2.9 m^2), and their scalability to smaller, higher-payload platforms remains an open question. A broader discussion of untethered soft systems and their challenges can be found in [32].

The preceding survey reveals an inherent trade-off between soft and conventional rigid robots, which presents designers with a fundamental dilemma: a choice between the efficiency, autonomy, and force capacity of rigid systems and the adaptability and versatility of soft, morphing systems. Hybrid robotics has emerged as a powerful synthesis, seeking to combine the "best of both worlds" by integrating soft, flexible, and rigid components into a single platform [33–35]. These hybrid platforms have demonstrated remarkable versatility, including the ability to seamlessly switch between distinct locomotion gaits and operational modes [36–38].

An important innovation within this hybrid paradigm is the implementation of variable-stiffness materials, which grant robots the ability to be rigid or compliant when needed, significantly expanding their functional envelope. Several technologies have been explored to this end. Shape-memory materials (SMMs), such as shape-memory alloys (SMAs), can be programmed to hold temporary shapes and revert to their original form upon thermal stimulation [39]. This principle has been used to create crawling microrobots [40, 41]. Another effective approach is particle jamming, where vacuum pressure is used to transition a granular material between a fluid-like and a solid-like state [42]. Jamming has been successfully integrated into crawling robots [43] and loop-shaped robots for combined locomotion and manipulation [44].

While effective, these methods have drawbacks. SMAs can have slow actuation cycles, and jamming systems require a constant vacuum source, complicating untethered designs. In this context, LMPAs have emerged as a highly promising alternative [45]. LMPAs offer several key advantages: a large stiffness variation between their solid and liquid phases, superior thermal conductivity for rapid phase transitions (e.g., Field's metal at 18 W/(mK) [46] versus 0.15–0.3 W/(mK) for SMPs [47]), and greater suitability for robust, untethered systems. These compelling properties led us to select LMPA-based variable stiffness (VS) as the core technology for our work.

Building upon this foundation, we present a novel hybrid robot capable of efficient motion, object manipulation, and traversal through highly obstructed environments, uniting mobility, autonomy, and flexibility within a single platform. This article substantially advances our previous work on the Self-Reconfigurable Soft-Rigid (2SR) robot [48] by introducing a refined mechanical design and a comprehensive control and planning framework. It is worth noting that fully general mobile manipulation in real-world clutter often requires three-dimensional (3D) mobility, including vertical displacement and out-of-plane deformation to accommodate uneven terrain, steps, and multilevel contact interactions. However, in this work, we focus on the planar case: in a rigid state, the robot operates as an efficient omnidirectional platform for planar navigation, and the proposed planner/control pipeline is formulated in a 2D workspace. In a flexible state, it can alter its morphology to perform full-body planar enclosure of objects or conform to environmental constraints. This choice simplifies implementation and modeling, enabling a clear proof-of-concept study of the variable-stiffness, shape-adaptive bridge, and the coupled motion-morphology planning problem, while necessarily limiting applicability to predominantly planar environments. In the Discussion, we outline how the proposed technology and planning framework can be extended toward 3D operation in future work, including richer shape models and terrain-aware feasibility constraints.

The implementation of this system required us to address several interconnected technical challenges, and our primary contributions are:

1. An improved robot design centered on a modular variable-stiffness bridge (VSB) composed of compact, independent LMPA-based units. This architecture achieves a 2.5-fold improvement in phase transition speed and superior power efficiency over the previous monolithic design, while simultaneously enhancing system robustness.

2. A comprehensive framework that integrates a novel hybrid kinematic model with a hierarchical "Motion & Morphology" (M&M) controller. The kinematic model, based on cardioid motion analysis, describes the robot's complex dynamics across both rigid and flexible states. This model enables the M&M controller to coordinate discrete stiffness transitions with continuous motion control, utilizing mode-specific Model Predictive Controllers (MPC) for precise trajectory tracking and a supervisory finite-state machine for reliable stiffness management.
3. The Voronoi-assisted Motion and Morphology Planning (VMMP) algorithm, a high-level planner that accounts for the robot's complex, high-dimensional (5D) configuration space, which encompasses its planar pose, variable morphology and multiple motion modes. VMMP enables autonomous navigation and shape adaptation of a 2SR robot in densely cluttered environments. The planner intelligently analyzes the environment to compute a sequence of critical configurations, balancing path feasibility with the robot's unique kinematic and morphological constraints.

2 | System Architecture and Design

A self-reconfigurable soft-rigid robot consists of two locomotion units (LUs) and a VSB. The units, equipped with omni wheels, house all electronics and power supply for autonomous operation. The VSB can change its compliance, enabling the robot to switch between various locomotion and deformation modes.

When developing a bridge, we followed Tonazzini et al.'s approach [49] that demonstrated a VS fiber composed of a silicone tube filled with low-melting-point alloy (LMPA) and wrapped by an enameled wire heater. LMPAs transition from solid to liquid state when heated above their melting temperature T_m, allowing the assembled structure to become soft. The previous design of a 2SR robot [48] featured a bridge with two independently controlled segments. Each segment measured 8 mm in diameter and 40 mm in length, with a layered structure consisting of a silicone rod (5 mm diameter), coiled enameled wire (0.1 mm diameter), and Field's metal (32.5% bismuth, 51% indium, 16.5% tin by weight; $T_m \approx 62^{\circ}$C, Young's modulus >3 GPa), all encapsulated in a silicone tube. The fabricated robot demonstrated shape-shifting capabilities and promising potential for grasping and manipulating objects.

However, this design has limitations, including slow phase transitions (>100 seconds), high power consumption (~ 9 V for each segment), and bending constraints. VS segments were joined through a rigid 30 mm plastic connector that restricted deformation in the middle of the bridge. To address these limitations, we propose a new bridge design incorporating a cable chain with a modular VS backbone. Compact VS modules reduce heating area and alloy volume, enabling faster transitions and lower power consumption. A single cable chain ensures uniform bending throughout the bridge while maintaining the ability to control segments independently by arranging modules in separate circuits. The modular approach enhances flexibility and robustness, facilitating length adjustments and easy replacement of failed or damaged modules.

2.1 | Modular Variable-Stiffness Bridge

The VSB consists of a cable chain structure that connects LUs, with chain nodes featuring internal channels to house VS modular units (MUs). Each MU follows the core principle of unitary VS segments but introduces several key improvements in design and fabrication.

The MU comprises a silicone rod (3 mm diameter) running through a Field's metal layer (10 mm length, 3 mm inner diameter, 5 mm outer diameter), encapsulated by plastic caps at both ends, all assembled within a silicone shell (5 mm inner, 6 mm outer diameter). Unlike the previous design, where the heater was positioned between the silicone rod and alloy, a copper wire (0.1 mm diameter) is now coiled around the silicone shell. This modification prevents wire damage during fabrication and enables easier heater replacement without destroying the alloy-containing section. Instead of external cables, brass caps are soldered to the heater and mounted at the unit's ends.

Each manufactured MU measures 20 mm in length and 7 mm in diameter. The fabrication process uses precision molding for the alloy layer and automated coiling to produce a 1.7Ω heater. This resistance was selected as a trade-off to enable faster phase transition at 1A while minimizing power consumption by requiring only 1.7 V. The assembly is finished with a protective silicone coating (for more details, see Section S1).

The bridge comprises two independently controlled segments, each containing four modules ($\leq 4 \cdot 1.7 = 6.8$ V). Modules are inserted between chain nodes, with brass caps pressing against copper contacts within node channels for electrical connectivity. At the middle chain node where segments meet, modules have no outward-facing brass caps to prevent electrical interference between segments. Terminal modules at LU junctions incorporate NTC thermistors for temperature monitoring. Each VS segment connects to an adjacent LU through four cables: two for the sensor and two for the heater (one from the terminal module, another from the middle node contact) to establish the control circuit. A calibration model translates resistance readings from the NTC thermistor into an internal temperature estimate for the alloy. On a higher level, a Finite-State Machine manages stiffness by controlling the heating and cooling cycles based on this temperature feedback. Additionally, the controller accounts for the alloy's thermal hysteresis by using distinct temperature thresholds for melting and solidification to ensure reliable transitions between the flexible and rigid states (for more details, see Section S2).

The cable chain limits the total bending of the bridge to π radians ($\pi/2$ per segment), a constraint that prevents collision between the LUs while preserving sufficient deformation capability. This modular architecture, which pairs the cable chain with a VS backbone, requires significantly less alloy than monolithic approaches. This reduction directly translates to faster phase transitions and lower power consumption. Experimental validation confirms these advantages: the average rigid-to-flexible transition occurred in 35.9 s, while the flexible-to-rigid transition took 47.1 s. This represents a 2.5-fold improvement in overall transition speed compared to the previous monolithic design (for more details, see Section S3).

2.2 | Locomotion Units

LUs are designed as self-contained, non-holonomic robots ($47 \times 47 \times 75.5$ mm). Each unit has two custom-made omni wheels with a radius of 10 mm, positioned on adjacent sides of the unit frame facing outwards. A castor wheel is used to create a three-point contact with the substrate and stabilize the unit's motion. Steel bars within the frame serve as weights to ensure solid wheel-ground contact.

Each LU is equipped with AS5600 encoders, a Li-ion battery (3.7V, 1000mAh) boosted to 9.6V, and an STM32-based controller. This controller operates brushless DC motors to drive the wheels and actuates a modular VS backbone inside the bridge. The signal captured from the segment's NTC thermistor is converted into temperature values that are used to generate appropriate PWM output to control the MU heaters. Communication with the central computer is established through a wireless serial board.

This configuration allows precise VSB manipulation in its soft state while maintaining three degrees of freedom when rigid, regardless of bridge shape. The complete 2SR robot structure is shown in Figure 1.

3 | Motion and Morphology Control

The dual capability of the 2SR robot to function as both an omnidirectional mobile platform and a deformable manipulator expands its potential applications. However, this versatility presents a unique challenge in developing a unified control framework that accommodates the distinct characteristics of both operational modes. This section introduces a hybrid kinematic model that seamlessly integrates rigid locomotion and soft manipulation, along with a control strategy enabling smooth transitions between modes. To facilitate the mathematical formulation, we establish the following key assumptions:

- The support surface is locally planar; roll/pitch and vertical displacement are neglected (planar $SE(2)$ locomotion). Hence, out-of-plane deformation, gravity-induced sag/torsion effects, and terrain contact feasibility are not modeled in the current formulation.
- VS segments are inextensible, that is, their length is constant.
- Flexible segments deform into constant-curvature arcs.
- LUs move independently when segments are flexible.
- The robot maintains omnidirectional mobility in a rigid state through strategically positioned omni wheels, independent of its configuration.

3.1 | Hybrid Kinematics

Given that the shape of the robot is not constant, defining its configuration is not trivial. Based on our constant-curvature assumption, each VSS configuration can be fully determined by three parameters: the position of one endpoint, the tangent direction at this endpoint, and the VSS curvature. Since both segments share a common endpoint at the bridge's approximate midpoint, we assign the robot's body frame $\{B\}$ at this location, oriented along the local tangent direction. This allows us to describe the robot's complete configuration using five generalized coordinates: two for position x_b, y_b, one for orientation θ_b, and two curvature values κ_1 and κ_2 (one for each segment s_1 and s_2) so that it can be expressed as $\mathbf{q} = [x_b, y_b, \theta_b, \kappa_1, \kappa_2]^{\mathrm{T}}$. With this configuration defined, the positions of the wheels can be computed from LU geometry.

3.1.1 | *Rigid State*

To analyze the robot's motion, it is essential to identify its velocities and the mechanisms generating them in each stiffness state. When rigid ($s_1 = s_2 = 0$), the 2SR agent behaves akin to a conventional omnidirectional robot.

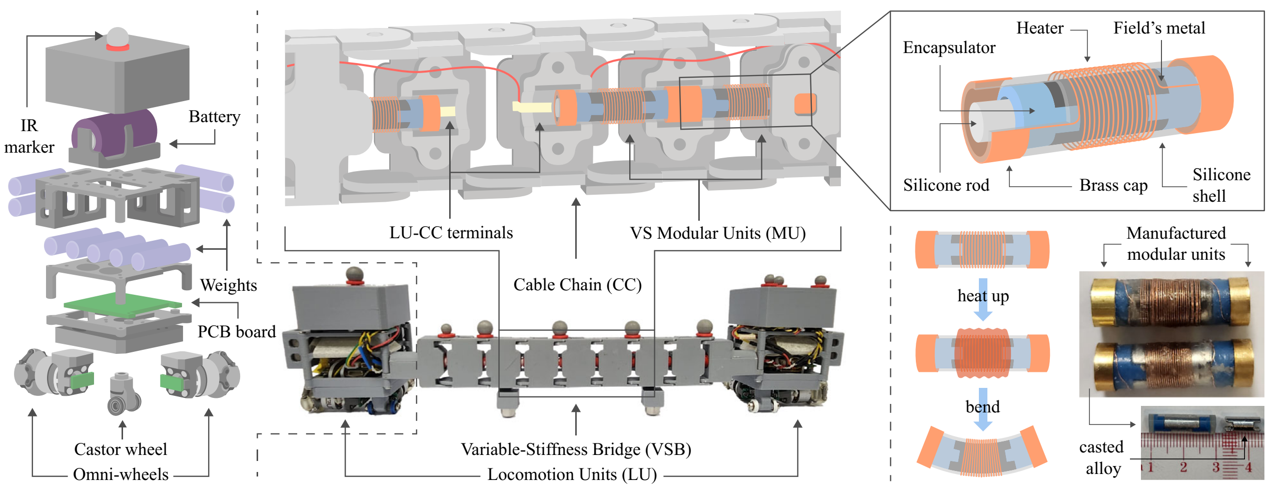

FIGURE 1 | Structural overview of the 2SR robot: exploded view of the locomotion unit showing its internal architecture; composition of the assembled variable-stiffness (VS) bridge with modular units forming a cable chain backbone; detailed view of a single VS modular unit showing its components and operating principle; photographs of manufactured components including the cast alloy layer and fully assembled module.

Then, its kinematics can be defined as

$$\dot{\mathbf{q}} = \underbrace{\overline{(s_1 \vee s_2)} \begin{bmatrix} \mathbf{R}_z(\theta_b) \\ 0 \end{bmatrix}}_{\mathbf{J}_r} \mathbf{u}_r \tag{1}$$

where $\mathbf{R}_z(\theta_b) \in \mathbb{R}^{3\times3}$ is a rotation matrix around the vertical axis of the global frame and $\mathbf{u}_r = [v_{bx}, v_{by}, \omega_b]^{\mathrm{T}}$ is a vector of robot's "rigid" control velocities associated with $\{B\}$.

3.1.2 | *Flexible States*

During flexible operation, LUs function as independent actuators. To prevent collisions between LUs, the cable chain bending is restricted to a half circle, constraining segment curvatures to $-\frac{\pi}{2l} \le \kappa_i \le \frac{\pi}{2l}$. It is observed that during the bending of the bridge, LUs trace a distinctive curve. The previous work [48] employed logarithmic spirals to model this motion, but it required separate functions for positive and negative curvatures, creating discontinuities at boundary conditions. Here, we use a cardioid model, which provides a single mathematical shape to approximate LU paths across all permissible curvature values:

$$x(\phi) = \rho \cos \phi, \quad y(\phi) = \rho \sin \phi \tag{2}$$

where $0 \le \phi \le 2\pi$ is the rolling angle, $\rho = 2r(1 - \cos \phi)$ is the cardioid's radius at ϕ, and r is the common radius of the two generating circles of the cardioid.

To fully comprehend the robot kinematics in a soft state, we categorize the operational modes into three distinct scenarios where different combinations of bending and motion occur. Each scenario is associated with a unique cardioid; see Figure 2:

1. One segment is flexible while the other remains rigid. The LU adjacent to the flexible segment is in motion.
2. One segment is flexible while the other remains rigid. The LU adjacent to the rigid segment is in motion.
3. Both segments are flexible, with either LU moving.

Through path analysis and curve fitting, we determine the cardioid radius r and the corresponding ϕ range for each scenario, as listed in Table 1. The VSS curvature exhibits an inverse linear relationship with the rolling angle ϕ, enabling reliable tracking of the robot's frame displacement using the cardioid equations.

TABLE 1 | Cardioids parameters.

Cardioid	r	$\phi^{\min}$	$\phi^{\max}$
1	0.021	2.42	3.87
2	0.049	2.19	4.09
3	0.043	1.73	4.56

The robot's motion in flexible states is controlled through "soft" velocities $\mathbf{u}_s = [v_1, v_2]^T$, where v_j represents the velocity of the j-th LU traversing a specific cardioid path.

This control approach differs fundamentally from the rigid state. By analyzing flexible modes independently and then integrating their contributions, we develop comprehensive kinematic equations governing the robot's movement.

Cardioid 1: $s_i = 1$, $s_{3-i} = 0$, $v_j \ne 0$, and $v_{3-j} = 0$; where $i, j \in [1, 2]$, $i = j$. Consequently, $\dot{x}_b = \dot{y}_b = \dot{\theta}_b = \dot{\kappa}_{3-i} = 0$.

The first flexible scenario is characterized by the motion of the j-th LU along a cardioid with velocity v_j, causing an adjacent flexible segment to bend while $\{B\}$ remains stationary. Curvature is derived through the rolling angle by mapping their corresponding ranges, $\Delta\kappa = \frac{\pi}{l}$ and $\Delta\phi_1 = \phi_1^{max} - \phi_1^{min}$:

$$\begin{cases} \kappa_i \approx -\dfrac{\pi}{2l} + \dfrac{\pi}{l\Delta\phi_1}(\phi_1^{max} - \phi_1) \\ \phi_1(\kappa_i) \approx \phi_1^{min} + \dfrac{l\Delta\phi_1}{\pi}\left(\dfrac{\pi}{2l} - \kappa_i\right) \end{cases} \tag{3}$$

The rolling angle rate is proportional to the speed of the object tracing the curve. Note that LU2 is located on the positive side of the x-axis of the frame, while LU1 is on the negative side. Therefore, a positive velocity of LU2 increases the curvature (and decreases ϕ), while a positive velocity of LU1 decreases the curvature (and increases ϕ).

Differentiating curvature in Equation (3) with respect to ϕ_1, we get

$$\dot{\phi}_1 = (-1)^{j-1}\frac{v_j}{\rho_1} \;\Rightarrow\; \dot{\kappa}_i = (-1)^j \underbrace{\frac{\pi}{l\Delta\phi_1\rho_1}}_{K_1(\kappa_i)} v_j \tag{4}$$

Cardioid 2: $s_i = 1$, $s_{3-i} = 0$, $v_j \ne 0$, and $v_{3-j} = 0$; where $i, j \in [1, 2]$ and $i \ne j$; $\dot{\kappa}_{3-i} = 0$.

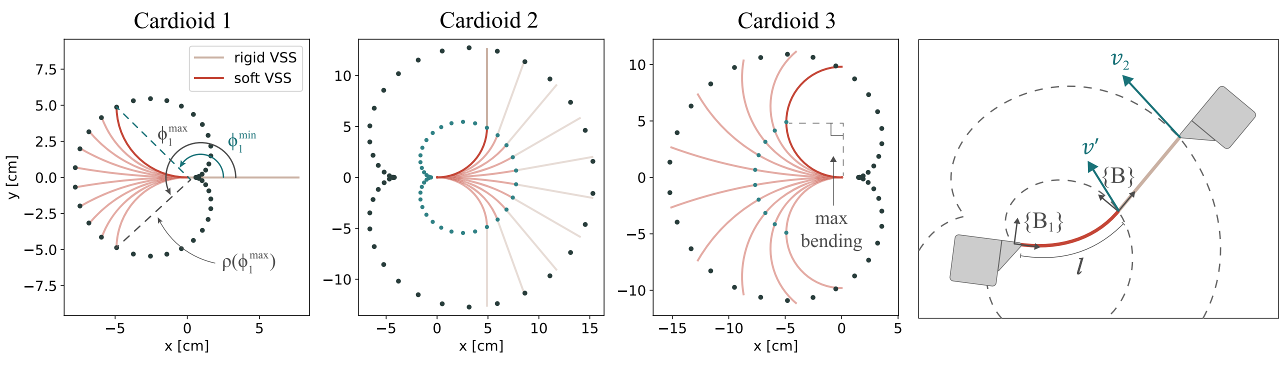

FIGURE 2 | Kinematic representation of the soft robot deformation and locomotion unit motion approximated by three distinct cardioid trajectories.

In this scenario, one segment remains flexible while the other is rigid, but unlike Cardioid 1, the moving LU is adjacent to the rigid segment. This configuration causes frame $\{B\}$ to follow the bending motion of the flexible segment. The LU in motion traces Cardioid 2, while the body frame traverses Cardioid 1 with its origin at the stationary LU. The frame body frame position can be determined through its location on Cardioid 1 using Equation (2):

$$\begin{bmatrix} \mathbf{p}_b \\ 1 \end{bmatrix} = \mathbf{T}_{bi} \begin{bmatrix} (-1)^{j-1}\rho_1 \cos\phi_1 \\ \rho_1 \sin\phi_1 \\ 1 \end{bmatrix} \tag{5}$$

where $\mathbf{p}_b = [x_b, y_b]^T$ is the body frame's position vector and $\mathbf{T}_{bi}$ represents the coordinate transformation from the stationary LU frame $\{B_i\}$ to global coordinates. The orientation of the frame $\{B_i\}$ is calculated as $\theta_{bi} = \theta_b + (-1)^i \kappa_i l$.

Figure 2 illustrates that the body frame traverses Cardioid 1 with velocity v', which differs from the LU velocity v_j along Cardioid 2. We can establish the relationship between these velocities by leveraging the fact that the curvature rate remains constant regardless of which cardioid we use for its derivation: $\dot{\kappa}_i = -\frac{\pi}{l\Delta\phi_1}\dot{\phi}_1 = -\frac{\pi}{l\Delta\phi_2}\dot{\phi}_2$. Then, using the definition of the rolling angle velocity from Equation (4), we obtain

$$v' = \underbrace{\frac{\Delta\phi_1}{\Delta\phi_2\rho_2}}_{\lambda_2(\kappa_i)}\rho_1 v_j \tag{6}$$

Now, differentiating Equation (5) with respect to ϕ_1 and substituting the rolling angle's derivative from Equation (6), we find the rate of the body frame's displacement:

$$\begin{bmatrix} \dot{x}_b \\ \dot{y}_b \end{bmatrix} = \underbrace{(-1)^{j-1}\frac{\partial \mathbf{p}_b}{\partial \phi_1}\lambda_2(\kappa_i)}_{\mathbf{J}_{j2}(\kappa_i,\theta_b)} v_j \tag{7}$$

The orientation of frame $\{B\}$ changes proportionally to the variation in segment curvature: $\Delta\theta_b = (-1)^i \Delta\kappa_i l$. Consequently, using the previously derived relationships for the curvature rate in Equation (4), we obtain

$$\dot{\theta}_b = lK_2(\kappa_i)v_j \tag{8}$$

Cardioid 3: $s_i = 1,\ s_{3-i} = 1,\ v_j \neq 0,\ v_{3-j} = 0,\ \dot{\kappa}_1 = \dot{\kappa}_2$.

In this scenario, both segments maintain flexibility while undergoing simultaneous deformation, resulting in equal curvature rates. The generalized coordinates and their derivatives follow the same principles established in the previous cases, with the key distinction being the synchronized bending of both segments. The frame position and orientation can be determined using the previously derived equations, accounting for the combined effect of dual-segment flexibility.

3.1.3 | *Unified Model*

Assembling Equations (4)–(8), we can express the kinematics of all soft states through the following unified Jacobian matrix:

$$\begin{gathered} \dot{\mathbf{q}} = \mathbf{J}(\mathbf{q},\mathbf{s})\mathbf{u} \\ \mathbf{J}(\mathbf{q},\mathbf{s}) = [\mathbf{J}_r, \mathbf{J}_s], \quad \mathbf{u} = [\mathbf{u}_r, \mathbf{u}_s]^{\mathrm{T}} \\ \mathbf{J}_s = \begin{bmatrix} s_2 & s_1 \\ s_2 & s_1 \\ s_2 & s_1 \\ s_1 & s_1 \\ s_2 & s_2 \end{bmatrix} \circ \begin{bmatrix} \mathbf{J}_{1n}(\kappa_2,\theta_b) & \mathbf{J}_{2n}(\kappa_1,\theta_b) \\ lK_n(\kappa_2) & lK_n(\kappa_1) \\ -K_m(\kappa_1) & K_n(\kappa_1) \\ -K_n(\kappa_2) & K_m(\kappa_2) \end{bmatrix} \\ (m,n) = \begin{cases} (3,3) & \text{if } s_1 \wedge s_2, \\ (1,2) & \text{otherwise} \end{cases} \end{gathered} \tag{9}$$

This kinematic model features nonholonomic constraints and coupling between the robot's pose and shape, particularly in the flexible states. A detailed analysis was performed to characterize the reachable configuration manifolds for each flexible mode. The analysis demonstrates that the fully flexible mode offers superior controllability, enabling decoupled rotation and translation and providing a connected, hole-free workspace. In contrast, the semi-flexible modes exhibit strong coupling between rotation and translation, which makes pure in-place rotation impossible and results in a reachable workspace with a significant excluded region near the origin (for more details, see Section S4). These inherent kinematic constraints highlight the distinct capabilities and limitations of each operational mode, underscoring the need for a control strategy that can prioritize the appropriate mode for a given task.

3.2 | Multimodal Motion and Shape Control

Having established the robot's operational modes through hybrid kinematics, we implement a comprehensive control strategy comprising four distinct MPC corresponding to each possible stiffness configuration $\mathbf{s} \in \mathbf{S}$, where $\mathbf{S} = \{[0,0],[1,0],[0,1],[1,1]\}$. Each controller follows the same framework while incorporating mode-specific kinematics. For a prediction horizon N, the MPC optimization problem is formulated as

$$\begin{array}{ll} \text{minimize} & \sum_{k=0}^{N}\tilde{\mathbf{q}}_k^{\mathrm{T}}\mathbf{Q}\tilde{\mathbf{q}}_k + \sum_{k=0}^{N}\mathbf{u}_k^{\mathrm{T}}\mathbf{R}\mathbf{u}_k \\ \text{subject to} & \tilde{\mathbf{q}}_k = \mathbf{q}_k - \mathbf{q}_{ref} \\ & \mathbf{q}_{k+1} = \mathbf{q}_k + \Delta t \mathbf{J}(\mathbf{q}_k,\mathbf{s}_k)\mathbf{u}_k \\ & |w_i| \leq w_{max},\ i = 1\ldots 4 \end{array} \tag{10}$$

where $\mathbf{q}_k$ is the robot's state vector, $\mathbf{q}_{ref}$ is the robot's reference state, $\mathbf{u}_k$ is the control velocity vector, $\mathbf{Q}$ and $\mathbf{R}$ are positive definite weighting matrices, $\mathbf{s}_k$ is the stiffness configuration, $\mathbf{J}(\mathbf{q}_k,\mathbf{s}_k)$ is the Jacobian defined in Equation (9), and w_i represents individual wheel velocities bounded by w_{max}.

To seamlessly integrate continuous motion control with discrete stiffness transitions, we implement a hierarchical Motion & Morphology (M&M) Controller. This supervisory framework operates through two key mechanisms: (1) stiffness state management, which triggers transitions when shape error crosses a threshold $\Delta\kappa_{min}$, and (2) motion coordination, which activates the appropriate mode-specific MPC controller. This approach optimizes system performance by maintaining segment rigidity by default and initiating transitions only when necessary for shape control.

4 | Voronoi-Assisted Motion and Morphology Planning

The M&M controller provides the low-level capability to execute specific configurations and motions by managing the robot's hybrid kinematics. However, to operate autonomously in complex environments, the robot requires a high-level planner that can reason about its goals and the surrounding space. The integration of shape adaptation significantly expands the configuration space to include five generalized coordinates, two stiffness states, and four possible motion modes. This expansion introduces the challenge of planning not only motion trajectories but also coordinated shape deformations and stiffness transitions, resulting in a high-dimensional planning problem that must be solved to navigate cluttered environments and interact with objects.

The ultimate planning goal is to enable the robot to traverse through cluttered environments and perform complex interaction tasks, such as the following:

- **Full-Body Enclosure**: Unlike traditional mobile robots that rely on specialized end effectors, the 2SR robot can use its entire deformable body to envelop an object, creating extended contact that enables pose regulation and robust coupling for subsequent planar transport. This approach is particularly effective for irregularly shaped items. Note that this enclosure is not a force-closure grasp and does not guarantee no-slip under all maneuvers. Experimental validation was conducted on various objects with a detailed analysis of the enclosure process (Section S5).
- **Enclosure-Based Transport**: After enclosure, the robot can re-stiffen and transport the object by locomotion while regulating object orientation. We analyzed how enclosure quality affects slip and tracking performance (Section S6).

To address the complexity of motion planning, we adopted a systematic decomposition approach that breaks down the problem into manageable components:

1. **Environment Analysis**: Voronoi diagrams are employed to identify potentially traversable narrow passages.
2. **Critical Point Path Planning**: Using the Voronoi structure, we determine feasible trajectories for three key points on the robot (front, middle, and rear) that define its fundamental shape during navigation.
3. **Configuration Fitting**: The method maps robot configurations to the identified point sequences, ensuring planned shapes respect the robot's kinematic constraints.
4. **Traverse Configuration Selection**: Finally, we identify a minimal configuration set that fully defines the traversal sequence while minimizing potential stiffness transitions.

4.1 | Voronoi Analysis

The first step involves analyzing the environment to identify potentially traversable narrow passages. We employ Voronoi diagrams, a fundamental geometric structure that partitions space based on proximity to obstacle boundaries. For our application, we define the Voronoi diagram $\mathcal{V}(\mathcal{O})$ for a set of obstacles $\mathcal{O}$.

Each obstacle in the workspace is defined as a polygon with a set of vertices $\mathcal{O}_i = \{\mathbf{p}_{i,1}, \mathbf{p}_{i,2}, \ldots, \mathbf{p}_{i,n_i}\}$, where $\mathbf{p}_{i,j} \in \mathbb{R}^2$ denotes the j-th vertex of the i-th obstacle, and n_i is the number of vertices in obstacle i. The complete workspace obstacle set is denoted as $\mathcal{O} = \{\mathcal{O}_1, \mathcal{O}_2, \ldots, \mathcal{O}_m\}$, where m is the total number of obstacles.

For an obstacle $\mathcal{O}_i \in \mathcal{O}$, its Voronoi cell $\mathcal{V}(\mathcal{O}_i)$ is the set of all points in the workspace that are closer to $\mathcal{O}_i$ than to any other obstacle:

$$\mathcal{V}(\mathcal{O}_i) = \left\{\mathbf{v} \in \mathbb{R}^2 \mid d(\mathbf{v}, \mathcal{O}_i) \leq d\left(\mathbf{v}, \mathcal{O}_j\right), \forall j \neq i\right\} \tag{11}$$

where $d(\mathbf{v}, \mathcal{O}_i)$ denotes the minimum Euclidean distance between point $\mathbf{v}$ and obstacle $\mathcal{O}_i$. A Voronoi diagram $\mathcal{V}(\mathcal{O})$ is the union of all cells $(\mathcal{V}(\mathcal{O}_i))_{\mathcal{O}_i \in \mathcal{O}}$.

The Voronoi diagram is used to build a weighted graph $\mathcal{G} = (\mathcal{V}, \mathbf{E})$, where edges $\mathbf{E}$ connect adjacent vertices in $\mathcal{V}$. Each vertex $\mathbf{v} \in \mathcal{V}$ has a clearance $c(\mathbf{v}) = \min_{\mathcal{O}_i \in \mathcal{O}} d(\mathbf{v}, \mathcal{O}_i)$ and an edge $\mathbf{e} \in \mathbf{E}$ with endpoints $(\mathbf{v}_1, \mathbf{v}_2)$ has length $l(\mathbf{e}) = ||\mathbf{v}_2 - \mathbf{v}_1||_2$ and clearance $c(\mathbf{e}) = \min(c(\mathbf{v}_1), c(\mathbf{v}_2))$.

To ensure practical traversability, multiple checks are performed along each edge by sampling a passage $\mathcal{S}_\mathbf{e}$ with k points: $\mathbf{p}_i = \mathbf{v}_1 + \frac{i}{k}(\mathbf{v}_2 - \mathbf{v}_1), \quad i \in \{0, 1, \ldots, k-1\}$ and verifying clearance at each point $\mathbf{p}_i$. We want to make sure that LUs can go through a passage. Therefore, a minimum clearance threshold is calculated as $\tau = a + \delta$, where a is the length of the LU side and δ is the safety margin.

Lemma 1. *A passage $\mathcal{S}_\mathbf{e}$ between vertices $\mathbf{v}_1$ and $\mathbf{v}_2$ is traversable if $\forall \mathbf{p}_i \in \mathcal{S}_\mathbf{e}$: $\mathbf{p}_i \cap \mathcal{O} = \varnothing$, $\min_{\mathbf{p}_i \in \mathcal{S}} c(\mathbf{p}_i) \geq \tau$, and there exists at least one continuous connection between $\mathcal{S}_\mathbf{e}$ and another traversable passage.*

Based on the set of traversable passages identified according to Lemma 1, we construct a subgraph $\widehat{\mathcal{G}} = (\widehat{\mathcal{V}}, \widehat{\mathbf{E}}) \subseteq \mathcal{G}$, where $\widehat{\mathbf{E}} = \{\mathbf{e} \in \mathbf{E} \mid \mathcal{S}_\mathbf{e} \text{is traversable}\}$ contains only edges corresponding to traversable passages and $\widehat{\mathcal{V}}$ consists of their associated vertices. This reduced graph $\widehat{\mathcal{G}}$ forms the basis for subsequent motion planning and analysis.

4.2 | Control Points Path Planning

Given the complex geometry of a flexible 2SR robot, we can simplify the path planning problem by focusing on three key characteristic points along the robot's length, see Figure 3: the *front* point $\boldsymbol{\xi}_f$ serving as the leading point during passage traversal (head or tail LU), the *middle* point $\boldsymbol{\xi}_m$ acting as the central reference point of the robot, and the *rear* point $\boldsymbol{\xi}_r$ functioning as the trailing point during traversal. These points are positioned along the robot's centerline (in a default configuration) such that $||\boldsymbol{\xi}_f - \boldsymbol{\xi}_m|| = ||\boldsymbol{\xi}_r - \boldsymbol{\xi}_m|| = \frac{L}{2}$, where L is the robot's length. This minimal set of points is sufficient to verify the feasibility of the robot's placement within narrow passages and serve as control points for subsequent configuration reconstruction.

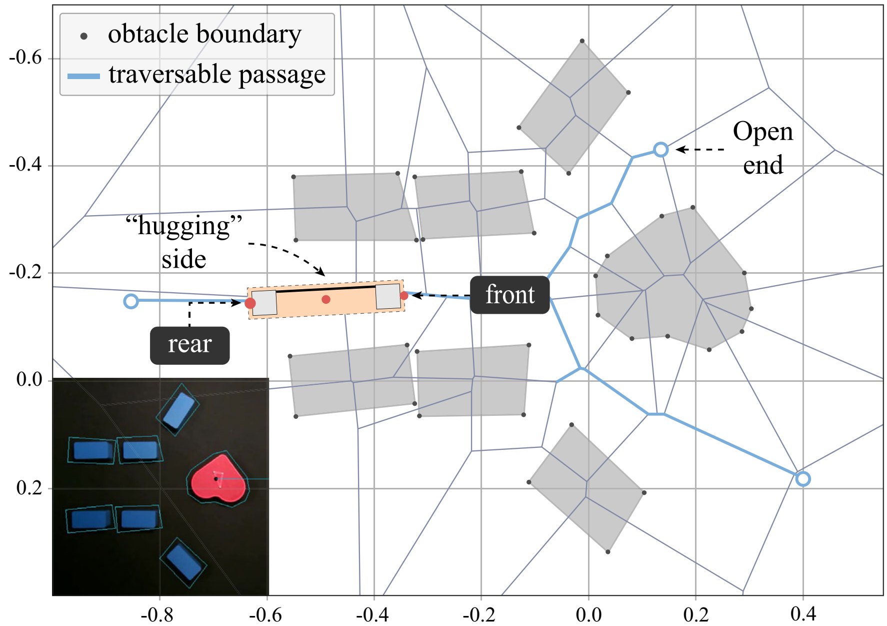

FIGURE 3 | Voronoi diagram of the highly cluttered environment with detected obstacles. The location of critical points on the robot is highlighted in red.

The selection of the front point depends on the environment. In most cases, either LU can be designated as the front. However, when the manipulandum is asymmetrically obstructed, the choice depends on the accessibility relative to the body frame in the target configuration that is determined as: $\mathbf{q}' = [\mathbf{x}_r', 0, 0]^{\mathrm{T}}$. The head LU is designated as front when the region corresponding to the negative x-axis of the body frame offers greater accessibility, while the tail LU is selected when the positive x-axis region is more accessible. This selection ensures that the robot's "hugging" front side will be properly oriented toward the manipulandum in the capture configuration.

For a given target configuration $\mathbf{q}'$, we first identify the global coordinates of the target control points:

$$\Xi' = \{\boldsymbol{\xi}_f(\mathbf{q}'), \boldsymbol{\xi}_m(\mathbf{q}'), \boldsymbol{\xi}_r(\mathbf{q}')\} \tag{12}$$

Each control point must be mapped to its nearest edge in the traversable graph $\widehat{\mathcal{G}}$. Let $d(\boldsymbol{\xi}, \mathbf{e})$ denote the distance from point $\boldsymbol{\xi}$ to edge $\mathbf{e}$. Then, the set of nearest edges for all target control points is defined as

$$\mathbf{E}' = \left\{ \mathbf{e}_i \mid \mathbf{e}_i = \arg\ \min_{\mathbf{e} \in \widehat{\mathbf{E}}} d(\boldsymbol{\xi}_i, \mathbf{e}), \boldsymbol{\xi}_i \in \Xi' \right\} \tag{13}$$

The robot's entry to the passage network is determined by finding the open-ended vertex closest to its initial position:

$$\mathbf{v}_0 = \arg\ \min_{\mathbf{v} \in \mathcal{V}'_{open}} ||\mathbf{v} - \mathbf{q}_0|| \tag{14}$$

where $\mathcal{V}'_{open} \subseteq \mathcal{V}'$ is the set of vertices with one incident edge.

Let $\mathbf{V}(\mathbf{E}')$ denote the set of vertices incident to edges in $\mathbf{E}'$. For each vertex $\mathbf{v} \in \mathbf{V}(\mathbf{E}')$, we define $\mathcal{P}_{\mathbf{v}}$ as the set of all possible paths from $\mathbf{v}_0$ to $\mathbf{v}$, where each path $\mathcal{P} \in \mathcal{P}_{\mathbf{v}}$ is a sequence of edges in $\widehat{\mathbf{E}}$. The optimal paths to all target vertices are determined using Dijkstra's algorithm:

$$\mathcal{P}^* = \left\{ \mathcal{P}_i^* \mid \mathcal{P}_i^* = \arg\ \min_{\mathcal{P} \in \mathcal{P}_{\mathbf{v}_i}} \sum_{\mathbf{e} \in \mathbf{P}} l(\mathbf{e}), \mathbf{v}_i \in \mathbf{V}(\mathbf{E}') \right\} \tag{15}$$

For each edge, $\mathbf{e} \in \mathbf{E}'$ we include only one endpoint ($\mathbf{v}_1$ or $\mathbf{v}_2$) to $\mathbf{V}(\mathbf{E}')$ based on which vertex yields the shorter path from $\mathbf{v}_0$. After determining the optimal path $\mathcal{P}_i^*$, we compute the projection point $\bar{\boldsymbol{\xi}}_i$ on the corresponding edge $\mathbf{e}_i$ that is closest to the control point $\boldsymbol{\xi}_i$:

$$\bar{\boldsymbol{\xi}}_i = \arg\ \min_{\mathbf{p} \in \mathcal{S}_{\mathbf{e}_i}} ||\mathbf{p} - \boldsymbol{\xi}_i||_2,\ \boldsymbol{\xi}_i \in \Xi', \mathbf{e}_i \in \mathbf{E}' \tag{16}$$

The final path is then augmented by adding an edge connecting vertex $\mathbf{v}$ to the projection point $\bar{\boldsymbol{\xi}}_i$.

4.3 | Path Coordination under Physical Constraints

While individual paths for control points provide general guidance through passages, maintaining the physical constraints of the robot's structure is crucial. The robot consists of three critical points connected by VS segments of fixed length. Throughout the motion, these distances must remain constant to prevent unrealistic stretching or compression of the segments.

We use the rear point's path $\mathcal{P}_r^*$ as the primary reference, as it represents the "pushing" end of the robot through the passage sequence. The front and middle points' paths are then adjusted to satisfy physical constraints. Let $\mathcal{S}_r = (\mathcal{S}_{\mathbf{e}})_{\mathbf{e} \in \mathcal{P}_r^*}$ be a sequence of equally spaced sample points along the edges in $\mathcal{P}_r^*$. For each point $\boldsymbol{\xi}_r(k) \in \mathcal{S}_r$, we determine the corresponding locations of the middle and front points $\boldsymbol{\xi}_m(k)$ and $\boldsymbol{\xi}_f(k)$ subject to the following constraints:

$$\begin{cases} d\widehat{\mathcal{G}}(\boldsymbol{\xi}_f(k), \boldsymbol{\xi}_r(k)) = L, \\ d\widehat{\mathcal{G}}(\boldsymbol{\xi}_m(k), \boldsymbol{\xi}_f(k)) = d\widehat{\mathcal{G}}(\boldsymbol{\xi}_m(k), \boldsymbol{\xi}_r(k)) = \frac{L}{2} \end{cases} \tag{17}$$

where $d\widehat{\mathcal{G}}(\cdot, \cdot)$ denotes the geodesic distance along edges in $\widehat{\mathcal{G}}$.

The adjustment of the front and middle points' paths is dynamically governed by the rear point's progression through the passages. At branching points where multiple edges are available, we first prioritize edges present in the guidance paths $\mathcal{P}_m^*$ and $\mathcal{P}_f^*$. When points are pushed beyond their guidance paths, the next edge connected to their last visited edge is selected. In cases where multiple options exist, we select edges incident to vertices with higher degree in $\widehat{\mathcal{G}}$.

4.4 | Paths Smoothing and Optimization

The final step in determining paths for the robot control points is refinement. Path planning through Voronoi analysis, while ensuring feasibility, often results in trajectories containing unnecessary fluctuations and sharp turns. These artifacts, inherent to Voronoi diagrams, can lead to jerky motions and excessive shape deformations of a 2SR robot. A smoothing step is therefore crucial to refine the raw paths while preserving their essential navigational properties and maintaining clearance constraints.

The smoothing process begins with geometric analysis of the path structure, treating it as a collection of straight sections. Each j-th section in $\mathcal{S}_i$, $i \in \mathbb{S}$, $\mathbb{S} = \{r, m, f\}$ is characterized by its direction vector $\rightarrow\mathbf{d}_{i,j}$ and length $l_{i,j}$. The smoothing strategy employs a two-phase approach.

The first phase focuses on section merging, targeting nearly parallel adjacent path sections. For two consecutive sections, we compute their directional similarity:

$$\cos\beta_{i,j} = \frac{\vec{\mathbf{d}}_{i,j} \cdot \vec{\mathbf{d}}_{i,j+1}}{||\vec{\mathbf{d}}_{i,j}|| \cdot ||\vec{\mathbf{d}}_{i,j+1}||} \tag{18}$$

When $\beta_{i,j} < \beta_{max}$, these sections are merged through cubic spline interpolation, it effectively eliminates small oscillations while maintaining the path's overall structure.

The second phase addresses zigzag patterns that typically emerge when the path navigates between multiple obstacles. For any three consecutive sections, we analyze the total direction change:

$$\Delta\beta_{i,j} = |\beta_{i,j} - \beta_{i,j+1}| \tag{19}$$

If $\Delta\beta_{i,j} < \Delta\beta_{max}$, we replace the zigzag pattern with a single straight section while preserving endpoint positions and ensuring clearance constraints are maintained.

Finally, we perform uniform resampling to generate equally spaced points along the smoothed paths $\mathcal{S}_r^*$, $\mathcal{S}_m^*$, and $\mathcal{S}_f^*$, ensuring they contain the same number of points. Implementation of this path optimization is illustrated in Figure 4.

4.5 | Fitting Configurations

After obtaining smoothed paths for the critical points, we need to determine the complete robot configurations that satisfy these paths while maintaining the kinematic constraints of a 2SR robot.

For each n-th point along the path, we seek to find the optimal robot configuration $\mathbf{q}_n$ that best matches the desired positions of control points while ensuring smooth transitions between consecutive states.

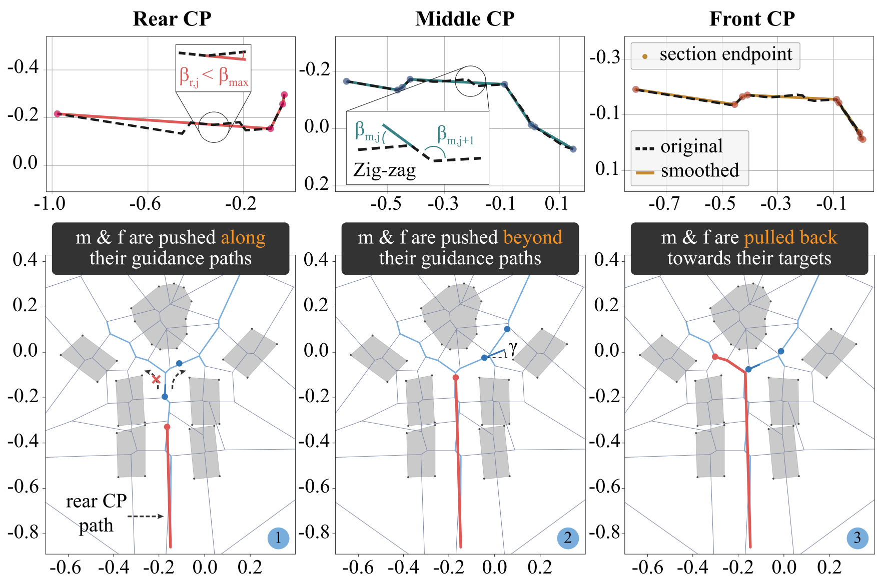

FIGURE 4 | Optimized paths for 2SR robot's control points (CP). Top: Comparison of paths before and after smoothing optimization. Bottom: Evolution of the robot's motion through the workspace, showing the Voronoi diagram and the coordinated movement of the three control points.

The optimization problem is formulated as

$$\begin{array}{ll} \underset{\mathbf{q}_n \in \mathbb{R}^5}{\text{minimize}} & \sum_{i \in \mathbb{S}} w_i ||\boldsymbol{\xi}_i(\mathbf{q}_n) - \mathcal{S}_i^*(n)||_2 + \tilde{\mathbf{q}}_n^{\mathrm{T}} \mathbf{W} \tilde{\mathbf{q}}_n + \\ & + \lambda_\theta |\theta_{b,n} - \gamma_n| + \lambda_\kappa \left(|\kappa_{1,n}| + |\kappa_{2,n}| \right) \\ \text{subject to} & \tilde{\mathbf{q}}_n = \mathbf{q}_n - \mathbf{q}_{n-1} \\ & |\kappa_{j,n}| \le \dfrac{\pi}{2l},\ j \in \{1, 2\} \end{array} \tag{20}$$

where $\mathbb{S} = \{f, m, r\}$ is the set of critical points and $\boldsymbol{\xi}_i(\mathbf{q}_n)$ represents the mapping from configuration space to the global position of the i-th control point.

The objective function balances multiple requirements through its components. The first term ensures accurate positioning of critical points, with weights w_i prioritizing the middle point's placement. The smoothness term penalizes large changes between consecutive configurations through a weighted quadratic form with $\mathbf{W}$ being a positive definite weighting matrix. The third term aligns the robot's orientation with the desired direction γ_n, computed as the tangent at $\mathcal{S}_m^*(n)$ pointing toward the tail LU. The final term minimizes absolute curvatures to reduce unnecessary bending

This constrained optimization problem can be solved sequentially along the path using Sequential Least Squares Programming (SLSQP), with each solution serving as the initial guess for the next point.

4.6 | Discretizing Crucial Configurations

After obtaining a configuration path, we must address a fundamental limitation. A physical 2SR robot cannot execute continuous shape changes with arbitrary precision in a flexible state, especially when target configurations are significantly distant from each other. Substantial planar displacements require omnidirectional motion of the robot in a rigid state.

Instead of attempting to find a continuous motion with a shape deformation trajectory, we identify a discrete set of key configurations that capture the essential characteristics of the planned motion. This set can then be sequentially supplied to the M&M controller for robot execution. This discretization process is critical for practical implementation while maintaining the path's navigational intent.

The selection of key configurations follows a mathematical framework based on three criteria. First, we perform curvature extrema analysis. Let $\kappa_j(n)$ be a curvature function for the j-th VS segment along the robot configuration path with a path length parameter n. We identify local extrema where

$$\frac{d\kappa_j}{dn} = 0 \, \text{and} \left| \frac{d^2\kappa_j}{dn^2} \right| > 0, \quad j \in 1, 2 \tag{21}$$

Specifically, we detect peaks and valleys where $|\kappa_j| > \eta$.

Second, we perform flat region detection by identifying regions of approximately constant curvature where

$$\frac{1}{\Delta n} \sum_{n=n_1}^{n_2} \left| \frac{d\kappa_j}{dn} \right| < \varepsilon \tag{22}$$

These regions represent constant shape configurations that the robot should maintain during motion. Third, we include configurations at spatial extrema: arg $\min_n \mathbf{p}(n)$ and arg $\max_n \mathbf{p}(n)$, where $\mathbf{p} = [x_b, y_b]^{\mathrm{T}}$ is a robot position vector.

After the initial set of crucial configurations $\mathcal{Q}$ is found, it is refined through a proximity filter to prevent redundancy:

$$\mathcal{Q}^* = \{\mathbf{q}_i \in \mathcal{Q} : ||\mathbf{p}_i - \mathbf{p}_{i+1}||_2 > d_{\min},\ \mathbf{p}_i \in \mathbf{q}_i \tag{23}$$

where $d_{\min}$ is a minimum distance threshold in the configuration space, ensuring that consecutive configurations are sufficiently distinct to warrant separate execution.

The resulting discrete sequence of robot configurations $\mathcal{Q}^* = \{\mathbf{q}_1, \mathbf{q}_2, \ldots, \mathbf{q}_k\}$ provides a set of waypoints that captures essential shape changes along the passage traversal path while minimizing unnecessary deformations; see Figure 5. We denote this comprehensive framework for integrated motion and morphological planning as *VMMP* (*Voronoi-assisted Motion and Morphology Planning*).

5 | Results

To validate the proposed design and control methodology, we fabricated and tested a 2SR robot prototype. The experimental platform consisted of a $2.78 \times 1.4 \times 1.4$ m metal frame workspace equipped with six OptiTrack cameras for high-precision motion capture and a ceiling-mounted RGB camera for visual monitoring. To ensure stable and repeatable locomotion, the arena's floor was covered with a non-slip silicone mat, which guarantees reliable traction. A heart-shaped object with three low-friction support wheels was used as a manipulandum. The conducted experiment, consisting of four trials, assessed the robot's ability to execute a complete operational sequence, which comprised three consecutive tasks:

(A) Traversing through the obstacles
(B) Full-body enclosure of the object
(C) Transporting the captured object along the path.

5.1 | Traversing through the Obstacles

Figure 6 illustrates the robot configuration sequences generated by the VMMP method across four distinct scenarios. The process begins with converting the workspace into a Voronoi diagram, which enables the identification of traversable passages (highlighted in blue). For each scenario, VMMP generates optimal paths $\mathcal{Q}^*$ comprising four to five key configurations, starting from the robot's default shape. As the robot encounters constricted areas, the method determines the minimum deformation needed for the robot to fit through the narrow spaces while maintaining adequate clearance. The resulting configuration sequences demonstrate smooth morphological transitions while ensuring collision-free navigation through the constrained environment.

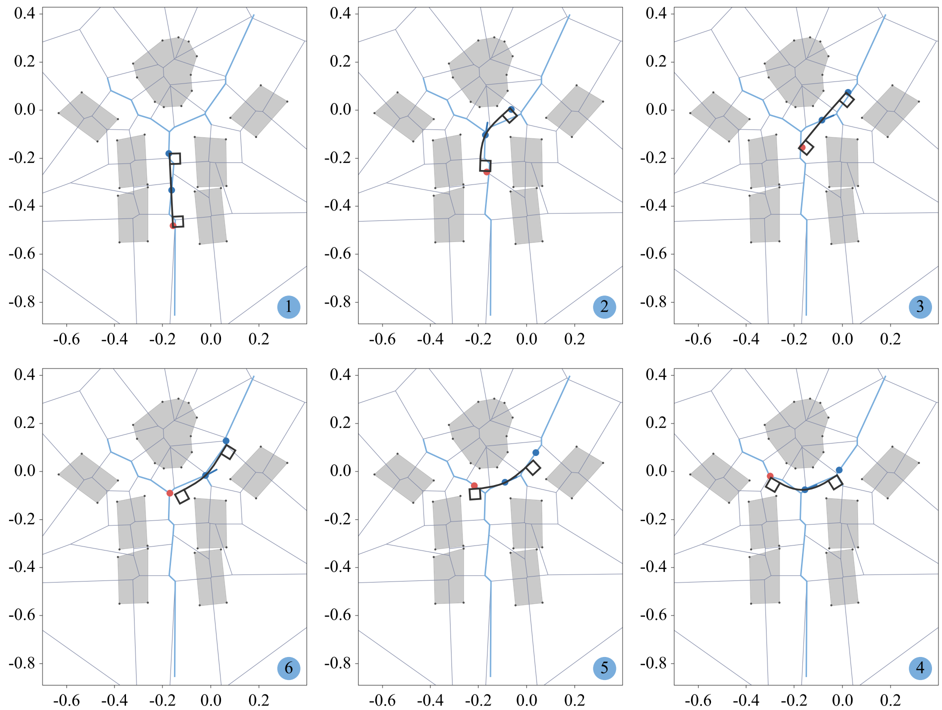

FIGURE 5 | Evolution of the robot's crucial configurations through the workspace. Configurations are reconstructed from the robot control points.

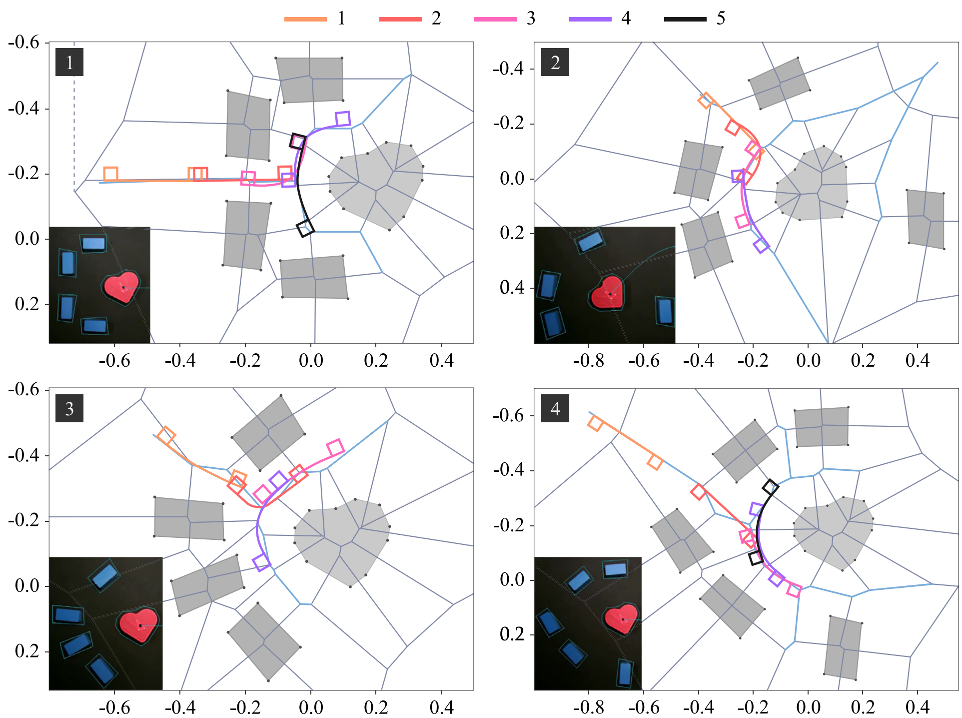

FIGURE 6 | Configuration sequences constructed by the Voronoi-assisted Motion and Morphology Planner (VMMP) for four different environment scenarios.

Figure 7 illustrates the robot's navigation through obstacles, demonstrating its dynamic stiffness switching, motion mode changes, and adaptive deformation. The execution process involves interpolating between key configurations in the VMMP-generated optimal path $\mathcal{Q}^*$ to ensure smooth motion, with each waypoint processed by the Motion and Morphology Controller. The quantitative plots in Figure 7 show robot state responses and velocity control inputs for trial "Heart 3."

In this scenario, the second segment underwent the most significant deformation, requiring 10 phase transitions (five rigid-to-soft and five soft-to-rigid), while the first segment switched stiffness

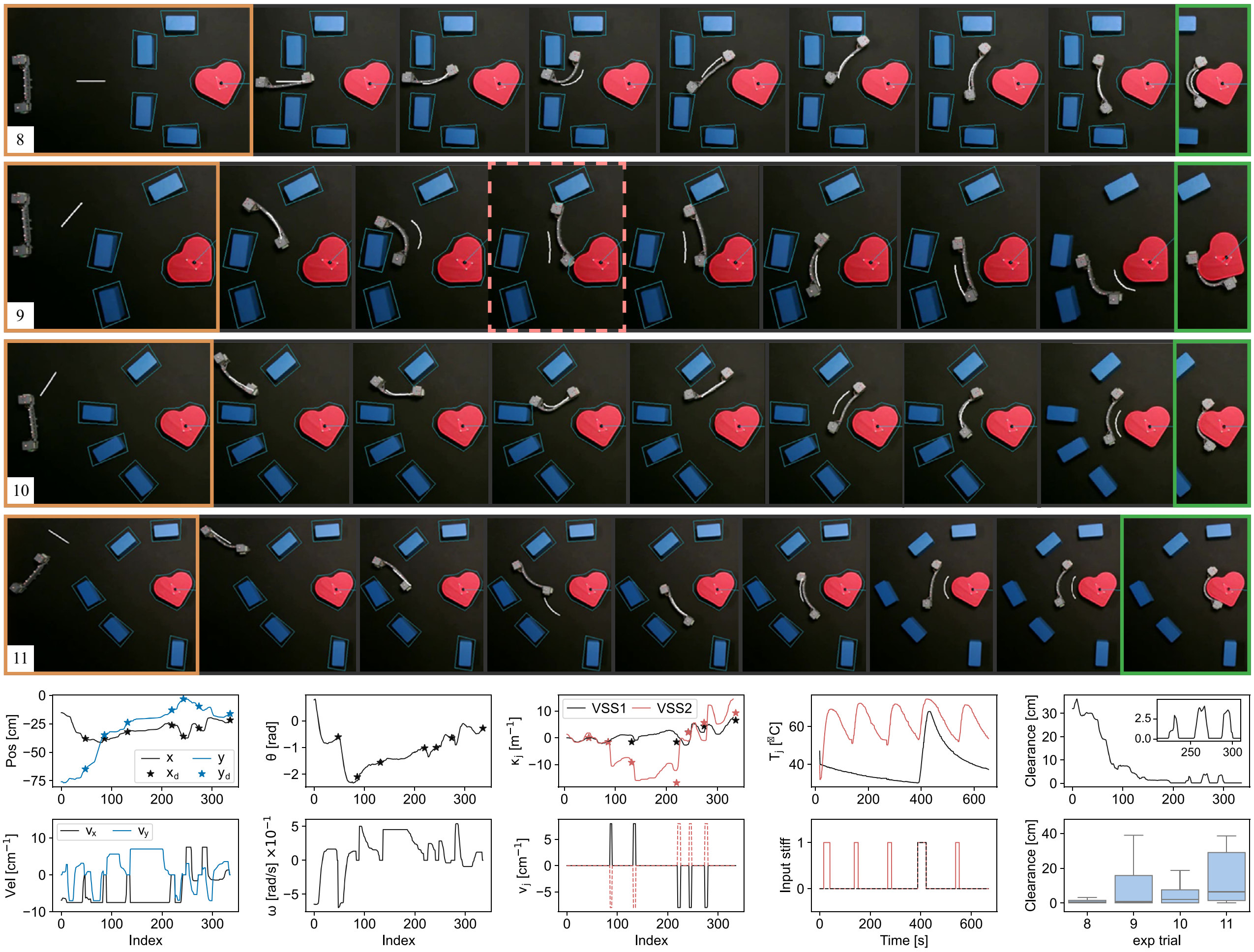

FIGURE 7 | Top: Time-lapse sequence showing the 2SR robot navigating through a cluttered environment using the VMMP motion and morphology planning method in four different scenarios. Bottom: System response data during experiments, including: robot configuration evolution, VSS temperature feedback, velocity and stiffness control inputs, and clearance measurements over time for trial "Heart 3" as well as clearance variations across all experiment trials.

only twice with a single deformation. Trial "Heart 4" presented the simplest case, requiring only one deformation in each segment. Other trials required 3–4 deformations (6–8 phase transitions) per segment. Completion times varied significantly: trial "Heart 3" took the longest at nearly 11 min, while trial "Heart 4" was the fastest at 2.5 min. Trials "Heart 1" and "Heart 2" were completed in 9.45 and 8.87 min, respectively.

When the robot navigates and deforms in the confined space between obstacles and the manipulandum, its LUs frequently approach the edges of obstacle buffer zones. This behavior is evident in the clearance plot in Figure 7, where values fluctuate considerably, often coming close to zero during deformation phases near obstacles. The 2SR robot generally managed these challenging zones effectively, with only a few buffer zone violations, such as during trial "Heart 2" (red frame in the execution sequence in Figure 7). Importantly, even in this instance, no physical collisions occurred, and neither the obstacles nor the manipulandum were disturbed despite the safety boundary violation.

The box plot in Figure 7 provides a summary of clearance measurements across all trials, reflecting the environmental complexity of each scenario. Trial "Heart 1," featuring the most congested workspace, exhibited the lowest average clearance, while trial "Heart 4," with its simpler configuration, maintained the highest clearance values.

5.2 | Full-Body Enclosure

The object retrieval process begins with the robot at the VMMP target, which defines the approach configuration for the full-body enclosure method. Figure 8 illustrates this process with a time-lapse sequence of the 2SR robot executing the final two steps: deformation into a capture configuration, followed by final positioning for contact. The quantitative plots for the "Heart 3" trial provide detailed insights into the robot's states and control inputs throughout this sequence.

First, the robot initiates a 13.5-second transition to a flexible state in its second segment. Once flexible, the robot uses "flexible" control velocities to adjust its segment curvature, conforming to the target shape required for enclosure. After achieving the desired shape, the robot undergoes a 47.7-second transition back to a rigid state. This rigidity allows for final adjustments to its overall pose to make contact with the object. During these rigid-flexible

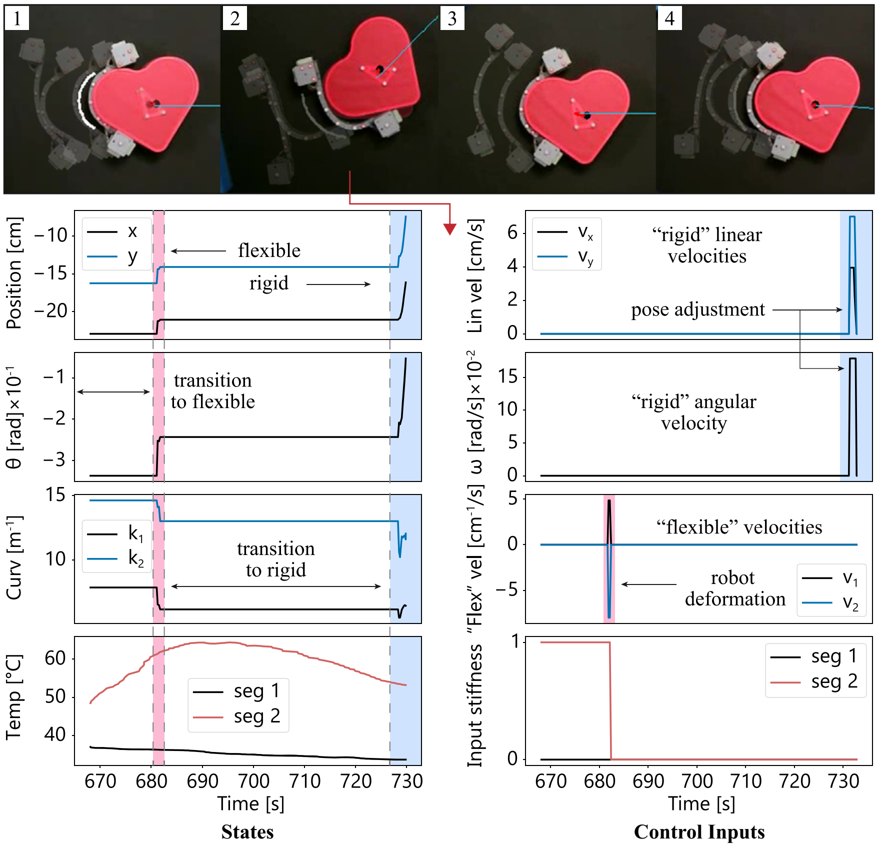

FIGURE 8 | Top: Time-lapse sequences of the 2SR robot executing a three-phase enclosure method on a heart-shaped object during the fixed-morphology experiment. Bottom: System responses during trial "Heart 3" showing robot states (pose, curvatures, and temperature feedback) and control inputs (target velocities and stiffness transition commands) throughout the enclosure process.

phase transitions, the robot remains stationary, resulting in constant state values and zero control inputs while the temperature of the second variable stiffness segment (VSS2) increases or decreases. Notably, in the rigid phase, minor fluctuations in the bridge curvatures are observed, which are attributed to the inherent residual flexibility of the robot's mechanical structure.

5.3 | Object Transportation

Figure 9 illustrates the performance of a robotic transportation task. Part (a) shows time-lapse sequences of the robot moving an object along a pre-defined reference path generated with a Bézier curve. Part (b) presents the system's velocity response during the "Heart 2" trial, plotting the heading (tangential) and lateral (normal) velocities. The manipulandum maintains a smooth heading velocity of $6\frac{cm}{s}$. The robot's heading velocity closely tracks this target, exhibiting corrective oscillations around the reference profile. The lateral velocity profiles demonstrate a symmetrical pattern with a minor offset between the robot and the object.

Figure 9c compares the spatial trajectories of the robot and the object against the reference path. The plot shows that the object adheres closely to the intended trajectory, confirming the success of the transportation task. Figure 9d plots the orientation of both the robot and the object over time. Their orientations remain closely aligned throughout the task, which indicates that the robot maintains a stable hold over the object during transport.

The contact quality has a significant influence on subsequent manipulation performance. In some instances, robot LUs may inadvertently disturb the object during enclosure, causing misalignment with the reference path and inducing oscillatory motion. These issues often stem from imperfect orientation or position overshooting at the capture configuration. The effect of these perturbations is evident in Figure 9e, which compares path tracking errors across different trials. The second trial exhibits the most significant oscillations at the start of the path, likely due to such a disturbance. Nevertheless, the data confirm that in all cases, the robot effectively stabilizes, damping the oscillations and converging onto the intended trajectory.

To quantify the relationship between enclosure quality and manipulation performance more rigorously, we introduce an enclosure index $L = L_{enc}/L_{obj}$ that measures the fraction of the object's perimeter contained within the robot's envelope. A detailed analysis across all trials and object shapes, provided in Supporting Information Section S6, reveals that E is a strong predictor of orientation regulation quality: a higher degree of body conformance is associated with lower rotational drift during transport and a significantly reduced final yaw error ($\rho = -0.92$), whereas its influence on translational drift is comparatively modest.

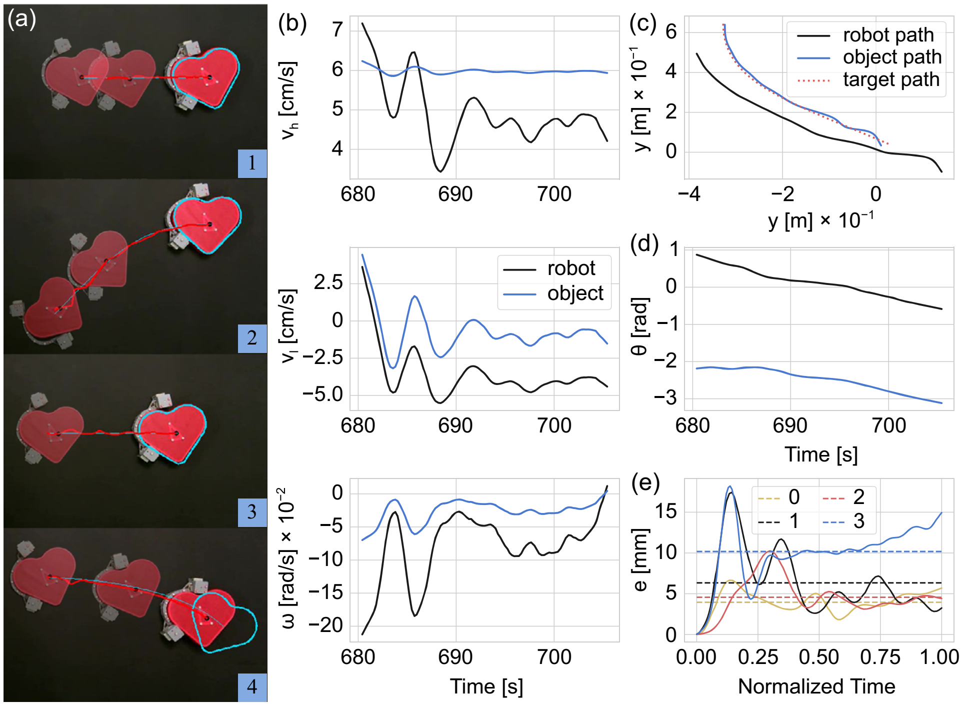

FIGURE 9 | (a) Time-lapse sequences of the 2SR robot transporting the object along the path. Second trial: (b) Control velocity inputs (heading, lateral, and rotational) for both the robot and the object; (c) Spatial trajectories of robot and object centroids, demonstrating path-following performance; (d) Comparison of robot-object orientation dynamics. (e) Time evolution of object tracking error across all trials.

6 | Discussion

This article introduced a comprehensive framework for autonomous mobile manipulation in cluttered planar environments, centered on a novel shape-shifting, variable-stiffness robot. Our approach integrates an improved 2SR robot design featuring a modular, LMPA-based VSB, which achieves a 2.5-fold increase in state transition speed and enhanced robustness with a hierarchical Motion and Morphology (M&M) control architecture. This controller leverages a hybrid kinematic model to seamlessly manage discrete stiffness transitions and continuous, mode-specific motion control, enabling the execution of complex configuration sequences. These sequences are generated by our high-level planner, the Voronoi-assisted Motion and Morphology Planner (VMMP), which effectively addresses the high-dimensional planning problem by decomposing it into environment analysis, multi-point pathfinding, and kinematically constrained configuration reconstruction.

Experimental validation demonstrated the system's efficacy in executing a complete operational sequence: autonomous navigation through densely packed obstacles, full-body grasping of an irregularly shaped object, and subsequent object transportation. The results confirm that the integration of our hardware design, control strategy, and planning algorithm enables the robot to dynamically adapt its morphology and stiffness to successfully navigate and interact within challenging, constrained spaces. By unifying efficient locomotion, adaptive morphology, and autonomous planning within a single untethered platform, this work presents a significant step toward a new paradigm for mobile manipulation. It demonstrates the viability of hybrid soft-rigid systems as a practical solution to the long-standing trade-off between the adaptability of soft robots and the performance of conventional rigid systems.

At the same time, the current design and modeling choices imply clear boundaries for real-world application. The underlying assumption of a planar surface and in-plane deformation means that the robot cannot address a large number of cases where vertical movement and out-of-plane deformation are necessary, such as overcoming steps, traversing uneven ground, or engaging with multi-level contacts. In such settings, additional factors become essential, including roll-pitch dynamics, stability margins, traction variability and slip, and gravity-induced torsion of the bridge, which are not captured by the present planar kinematic and planning formulation. Extending the proposed technology toward more general 3D environments, therefore, requires both hardware and modeling adaptations. At the hardware level, the "two locomotion units + variable-stiffness bridge" morphology can be retained while replacing omnidirectional wheels with terrain-capable mobility modules (e.g., suspension wheels, tracked bases, or other mechanisms) to provide reliable contact on uneven ground and redesigning the bridge so that it to be able to bend around more than one axis. At the modeling level, the bridge representation must be augmented to include out-of-plane curvature, torsion, and gravity and contact effects, as well as the feasibility checks must be expanded to include support-contact and stability constraints such as friction margins and tip-over avoidance.

Another practical consideration is how the environment should be represented for planning in real-world scenarios. In this work, we used a Voronoi graph because it simplifies pathfinding and highlights the core contribution of the VMMP pipeline.

However, the proposed method is not fundamentally tied to this choice, which is important since real deployments often rely on imperfect sensing (e.g., depth cameras, point clouds) that produce partial, noisy, and occluded observations. The Voronoi-based component of VMMP can be replaced by a map derived from real-world sensing without disabling downstream configuration reconstruction or control. For example, point-cloud observations can be converted into an occupancy representation or a distance field (e.g., ESDF), allowing the planner to query obstacle clearance and perform collision checking in a manner analogous to Voronoi clearance while retaining the same decomposition into (i) global path generation, (ii) waypoint selection, and (iii) kinematically constrained configuration fitting. The same modular substitution works in 3D; a voxel map or 3D ESDF can be used for clearance-aware planning, leaving the subsequent waypoint and fitting stages intact.

In future work, we aim to explore several promising directions. First, reinforcement learning approaches will be investigated to better capture the complex non-linear behavior of the robot that is not fully represented in analytical models. Second, we plan to leverage the robot's combination of conforming ability and mobility for active environment exploration. In this work, we intentionally use a conservative, collision-avoidance planner to keep the planning problem well-defined and to enable clear, repeatable evaluation of the proposed VMMP pipeline under structured conditions. However, the inherent conformability of the robot's design suggests that it can safely accommodate mild, distributed contact and, in some cases, use contact to guide motion when operating in tight clutter. Therefore, the current strict collision-free planning can be relaxed and replaced by contact-tolerant navigation and exploration strategies that allow controlled interaction with the environment (e.g., bounded contact forces and controlled sliding), improving robustness to sensing uncertainty while simultaneously collecting contact-rich information during exploration. Third, we plan to extend the system toward more general 3D operation by integrating terrain-capable locomotion modules, incorporating out-of-plane deformation modeling and supporting feasibility constraints (stability, contact, slip), and adopting sensing-derived 3D environment representations for clearance reasoning and replanning. Finally, we plan to extend the system to multi-agent scenarios, studying how multiple 2SR robots can cooperatively accomplish more complex tasks. These developments will further expand the potential applications of this versatile robotic platform in challenging real-world environments.

Acknowledgments

This work was also supported in part by the PolyU FENG Intra-Faculty Interdisciplinary Project under grant WZ8B.

Funding

This study was supported by the Research Grants Council (RGC) (15231023).

Conflicts of Interest

The authors declare no conflicts of interest.

Data Availability Statement

The data that support the findings of this study are available from the corresponding author upon reasonable request.

References

1. N. Ghodsian, K. Benfriha, A. Olabi, V. Gopinath, and A. Arnou, “Mobile Manipulators in Industry 4.0: A Review of Developments for Industrial Applications,” *Sensors* 23, no. 19 (2023): 8026–8026.

2. P. Ben-Tzvi, A. A. Goldenberg, and J. W. Zu, “Design and Analysis of a Hybrid Mobile Robot Mechanism With Compounded Locomotion and Manipulation Capability,” *Journal of Mechanical Design* 130 (2008): 7.

3. J. Laber, R. Thamma, and E. Kirby, “IJISET - International Journal of Innovative Science,” *Engineering & Technology* 7, no. 8 (2020): 63–70.

4. A. Gunatilake, L. Piyathilaka, A. Tran, V. K. Vishwanathan, K. Thiyagarajan, and S. Kodagoda, “Stereo Vision Combined With Laser Profiling for Mapping of Pipeline Internal Defects,” *IEEE Sensors Journal* 21, no. 10 (2021): 11926–11934.

5. Y.-S. Chen and J.-G. Juang, in *2009 ICCAS-SICE* (IEEE, 2009), 3199–3204.

6. M. Bjelonic, N. Kottege, T. Homberger, P. Borges, P. Beckerle, and M. Chli, “Weaver: Hexapod Robot for Autonomous Navigation on Unstructured Terrain,” *Journal of Field Robotics* 35, no. 7 (2018): 1063–1079.

7. A. Elfes, R. Steindl, F. Talbot, et al., “The Multilegged Autonomous Explorer (MAX),” in 2017 IEEE International Conference on Robotics and Automation (ICRA), (IEEE, 2017), 1050–1057.

8. S. Mintchev and D. Floreano, “Adaptive Morphology: A Design Principle for Multimodal and Multifunctional Robots,” *IEEE Robotics & Automation Magazine* 23, no. 3 (2016): 42–54.

9. H. Hauser, “Resilient Machines through Adaptive Morphology,” *Nature Machine Intelligence* 1, no. 8 (2019): 338–339.

10. B. T. Wilcox, J. Joyce, and M. D. Bartlett, “Rapid and Reversible Morphing to Enable Multifunctionality in Robots,” *Advanced Intelligent Systems* 7 (2024): 7.

11. A. P. Sabelhaus, J. Bruce, K. Caluwaerts, et al., “System Design and Locomotion of SUPERball, an Untethered Tensegrity Robot,” in 2015 IEEE International Conference on Robotics and Automation (ICRA), (IEEE, 2015), 2867–2873.

12. J. Petrš, R. Kobayashi, F. van Diggelen, H. Nabae, K. Suzumori, and D. Floreano, “Evolutionary Codesign and Fabrication of Tensegrity Joints with Integrated Pneumatic Artificial Muscles,” *Advanced Intelligent Systems* 7 (2025): 9.

13. M. Polzin, Q. Guan, and J. Hughes, “Robotic Locomotion through Active and Passive Morphological Adaptation in Extreme Outdoor Environments,” *Science Robotics* 10 (2025): 99.

14. S. Li, R. Batra, D. Brown, et al., “Particle Robotics Based on Statistical Mechanics of Loosely Coupled Components,” *Nature* 567 (2019): 7748–7361.

15. Y. Xi, T. J. Jones, R. Huang, T. Marzin, and P.-T. Brun, arXiv preprint arXiv:2404.10614 (2024).

16. Z. Wang and V. Kumar, “Object Closure and Manipulation by Multiple Cooperating Mobile Robots,” in Proceedings 2002 IEEE International Conference on Robotics and Automation (Cat. No.02CH37292), Volume 1, (IEEE, 2002), 394–399.

17. F. Bertoncelli, M. Selvaggio, F. Ruggiero, and L. Sabattini, “Task-Oriented Contact Optimization for Pushing Manipulation With Mobile Robots,” in 2022 IEEE/RSJ International Conference on Intelligent Robots and Systems (IROS), (IEEE, 2022), 1639–1646.

18. F. Bertoncelli and L. Sabattini, “Streamlining Object Pushing: Behavior Tree-Based Coordination of Control and Planning,” in 2024 IEEE/RSJ International Conference on Intelligent Robots and Systems (IROS), (IEEE, 2024), 5203–5210.

19. M. Kulkarni, H. Nguyen, and K. Alexis, "The Reconfigurable Aerial Robotic Chain: Shape and Motion Planning," *IFAC-PapersOnLine* 53, no. 2 (2020): 9295.

20. H. Zhi, B. Zhang, J. Qi, et al., "Non-Prehensile Object Transport by Nonholonomic Robots Connected by Linear Deformable Elements," *IEEE Robotics and Automation Letters* 9 (2024): 8651–8658.

21. K. Son, K. Bowal, K. Kim, L. Mahadevan, and H.-Y. Kim, "Emergent Functional Dynamics of Link-Bots," *Science Advances* 11, no. 19 (2025): eadu8326.

22. A. Sarker, T. U. Islam, and M. R. Islam, "A Review on Recent Trends of Bioinspired Soft Robotics: Actuators, Control Methods, Materials Selection, Sensors, Challenges, and Future Prospects," *Advanced Intelligent Systems* 7 (2024): 3.

23. O. Rabaux and C. Jérôme, "Bioinspired Morphing Mechanisms for Soft Systems: A Review," *Advanced Intelligent Systems* 7 (2024): 2.

24. M. Sun, C. Tian, L. Mao, et al., "Reconfigurable Magnetic Slime Robot: Deformation, Adaptability, and Multifunction," *Advanced Functional Materials* 32, no. 26 (2022): 2112508.

25. L. V. Nguyen, H. Kim, K. T. Nguyen, F. Alambeigi, and V. A. Ho, "Adaptable Cavity Exploration: Bioinspired Vibration-Propelled PufferFace Robot with a Morphable Body," *Science Advances* 11, no. 18 (2025): eads3006.

26. T. Wang, J. Zhang, G. Zhao, Y. Li, J. Hong, and M. Y. Wang, "An Inchworm-Inspired Rigid-Reinforced Soft Robot With Combined Functions of Locomotion and Manipulation," in 2018 IEEE/ASME International Conference on Advanced Intelligent Mechatronics (AIM) (IEEE, IEEE, 2018), 1087–1091.

27. A. Yin, H.-C. Lin, J. Thelen, B. Mahner, and T. Ranzani, "Combining Locomotion and Grasping Functionalities in Soft Robots," *Advanced Intelligent Systems* 1, no. 8 (2019): 1900089.

28. P. Wharton, T. L. You, G. P. Jenkinson, et al., "Tetraflex: A Multigait Soft Robot for Object Transportation in Confined Environments," *IEEE Robotics and Automation Letters* 8, no. 8 (2023): 5007–5014.

29. M. T. Tolley, R. F. Shepherd, B. Mosadegh, et al., "A Resilient, Untethered Soft Robot," *Soft Robotics* 1, no. 3 (2014): 213–223.

30. X. Huang, Z. J. Patterson, A. P. Sabelhaus, et al., "Design and Closed-Loop Motion Planning of an Untethered Swimming Soft Robot Using 2D Discrete Elastic Rods Simulations," *Advanced Intelligent Systems* 4 (2022): 10.

31. N. S. Usevitch, Z. M. Hammond, M. Schwager, A. M. Okamura, E. W. Hawkes, and S. Follmer, "An Untethered Isoperimetric Soft Robot," *Science Robotics* 5, no. 40 (2020): eaaz0492.

32. S. I. Rich, R. J. Wood, and C. Majidi, "Untethered Soft Robotics," *Nature Electronics* 1, no. 2 (2018): 102–112.

33. H. C. Lee, N. Elder, M. Leal, et al., "A Fabrication Strategy for Millimeter-Scale, Self-Sensing Soft-Rigid Hybrid Robots," *Nature Communications* 15 (2024): 1.

34. L. Paternò, G. Tortora, and A. Menciassi, "Hybrid Soft–Rigid Actuators for Minimally Invasive Surgery," *Soft Robotics* 5, no. 6 (2018): 783–799.

35. H.-T. Lin, G. G. Leisk, and B. Trimmer, "GoQBot: A Caterpillar-Inspired Soft-Bodied Rolling Robot," *Bioinspiration & Biomimetics* 6, no. 2 (2011): 026007.

36. C. Liu, O. Edwards, K. Althoefer, K. Zhang, and H. Godaba, "An Electro-Pneumatic Shape-Morphing Rolling Robot With Variable Locomotion Modes," in 2022 IEEE 5th International Conference on Soft Robotics (RoboSoft), (IEEE, 2022), 715–721.

37. R. J. Lock, S. C. Burgess, and R. Vaidyanathan, "Multi-Modal Locomotion: From Animal to Application," *Bioinspiration & Biomimetics* 9, no. 1 (2013): 011001.

38. M. Kovač, O. Fauria Wassim-Hraiz, J.-C. Zufferey, and D. Floreano, "The EPFL JumpGlider: A Hybrid Jumping and Gliding Robot With Rigid or Folding Wings," in 2011 IEEE International Conference on Robotics and Biomimetics, (IEEE, 2011), 1503–1508.

39. Z. Li, X. Chu, X. Hu, Z. Zhang, N. Li, and J. Li, "Variable Stiffness Methods for Robots: A Review," *Smart Materials and Structures* 33, no. 6 (2023): 063002.

40. J.-S. Koh, S.-M. An, and K.-J. Cho, Finger-Sized Climbing Robot Using Artificial Proleg, in 2010 3rd IEEE RAS & EMBS International Conference on Biomedical Robotics and Biomechatronics, (IEEE, 2010), 610–615.

41. B. Kim, M. G. Lee, Y. P. Lee, Y. Kim, and G. Lee, "An Earthworm-Like Micro Robot Using Shape Memory Alloy Actuator," *Sensors and Actuators A: Physical* 125, no. 2 (2006): 429–437.

42. H. M. Jaeger, "Celebrating Soft Matter's 10th Anniversary: Toward Jamming by Design," *Soft Matter* 11, no. 1 (2015): 12–27.

43. E. Steltz, A. M. Mozeika, J. Rembisz, N. Corson, and H. M. Jaeger, "Jamming as an Enabling Technology for Soft Robotics," *Proceedings of SPIE* 7642 (2010): 764225.

44. M. A. Karimi, V. Alizadehyazdi, H. M. Jaeger, and M. Spenko, "A Self-Reconfigurable Variable-Stiffness Soft Robot Based on Boundary-Constrained Modular Units," *IEEE Transactions on Robotics* 38, no. 2 (2021): 1–12.

45. B. E. Schubert and D. Floreano, "Variable Stiffness Material Based on Rigid Low-Melting-Point-Alloy Microstructures Embedded in Soft Poly(dimethylsiloxane) (PDMS)," *RSC Advances* 3, no. 46 (2013): 24671.

46. A. Lipchitz, G. Harvel, and T. Sunagawa, "Experimental Investigation of the Thermal Conductivity and Viscosity of Liquid In-Bi-Sn Eutectic Alloy (Field's Metal) for Use in a Natural Circulation Experimental Loop," in Proceedings of ICONE-23/23rd International Conference on Nuclear Engineering, (ASME, 2015).

47. C. Liu, H. Qin, and P. T. Mather, "Review of Progress in Shape-Memory Polymers," *Journal of Materials Chemistry* 17, no. 16 (2007): 1543–1558.

48. L. Labazanova, S. Peng, L. Qiu, H.-Y. Lee, T. Nanayakkara, and D. Navarro-Alarcon, "Self-Reconfigurable Soft-Rigid Mobile Agent With Variable Stiffness and Adaptive Morphology," *IEEE Robotics and Automation Letters* 8, no. 3 (2023): 1643–1650.

49. A. Tonazzini, S. Mintchev, B. Schubert, B. Mazzolai, J. Shintake, and D. Floreano, "Variable Stiffness Fiber with Self-Healing Capability," *Advanced Materials* 28, no. 46 (2016): 10142–10148.

Supporting Information

Additional supporting information can be found online in the Supporting Information section.